The proteasome activator PA200 regulates tumor cell invasion

Ayse Seda Yazgili[1*], Dušan Živković[2,3**], Angelique Sanchez Dafun[2,3], Georgia G. Giotopoulou[1], Sabine Behrend[1], Frauke Koops[4], Linda Zemke[4], Elvira Stacher-Priehse[5], Torsten Goldmann[4], Norbert Reiling[4], Georgios T. Stathopoulos[1,6], Julien Marcoux[2,3], Marie-Pierre Bousquet[2,3#], Silke Meiners[1,4,7#]

[1]*Comprehensive Pneumology Center (CPC), University Hospital of the Ludwig-Maximilians-University (LMU) and Helmholtz Center Munich, Member of the German Center for Lung Research (DZL), Max-Lebsche Platz 31, 81377, Munich, Germany*

[2]*Institut de Pharmacologie et de Biologie Structurale (IPBS), Université de Toulouse, CNRS, Université Toulouse III - Paul Sabatier (UPS), Toulouse, France.*

[3]*Infrastructure Nationale de Protéomique, ProFI, FR 2048, Toulouse, France.*

[4]*Research Center Borstel/Leibniz Lung Center, Airway Research Center North (ARCN), Member of the German Center for Lung Research (DZL), 23845, Borstel, Germany*

[5]*Asklepios Lung Clinic Munich-Gauting, 82131, Gauting, Germany, Member of the German Center for Lung Research (DZL)*

[6]*School of Medicine, University of Cyprus, 2029 Aglantzia, Nicosia, Cyprus*

[7]*Institute of Experimental Medicine, Christian-Albrechts University, Kiel, Germany*

**Present Address: The CRUK Scotland Institute, Garscube Estate, Switchback Road, Bearsden, Glasgow, G61 1BD, United Kingdom*

***Present Address: University of Oxford, Department of Biology, South Parks Road, Oxford OX1 3RB, United Kingdom.*

 # to whom correspondence should be addressed:

Silke Meiners, PhD

Research Center Borstel/Leibniz Lung Center

Parkallee 1-40, 23845 Borstel, Germany

Email: smeiners@fz-borstel.de

Marie-Pierre Bousquet, PhD

Institut de Pharmacologie et de Biologie Structurale (IPBS)

Université Toulouse III - Paul Sabatier (UPS)

31077 Toulouse, France

Email: Marie-Pierre.Bousquet@ipbs.fr

ABSTRACT

The proteasome is a well-identified therapeutic target for cancer treatment but the efficacy of proteasome inhibitors for solid tumors is severely hampered by cytotoxic side effects due to broad proteasome inhibition in non-tumor tissues. We and others observed significant upregulation of proteasome activator 200 (PA200) specifically in non-small cell lung cancer (NSCLC) tissues correlating with poor prognosis. To understand the functional role of PA200, we genetically depleted PA200 in two different NSCLC cell lines and characterized its functional effects *in vitro* and *in vivo.* Of note, we observed a striking disparity in proteasome regulation, cellular growth, and transcriptome regulation upon deletion of PA200 in the two lung cancer cell lines. A common response to PA200 depletion, however, was the concerted impairment of tumor cell migration and invasion *in vitro* and diminished flank tumor growth *in vivo*. These data strongly suggest that the function of PA200 in tumor cells depends on the cellular context but has a conserved effect on tumor cell migration. Furthermore, using an *in vitro* drug screening system with purified 20S and recombinantly expressed PA200, we were able to identify a PA200 inhibitor. This compound inhibits the activity of PA200-proteasome complexes but only marginally interferes with the catalytic activity of the 20S proteasome core. The drug showed inhibitory activity in cell extracts and reduced the invasive capacity of A549 lung cancer cells. Taken together, our data uncover PA200 as a potential target for lung cancer therapy and identify Prest2-M17 as a potential PA200 inhibitor.

INTRODUCTION

The proteasome is a well-identified therapeutic target for cancer treatment. It acts as the main protein degradation system in the cell and degrades key mediators of cell growth, migration and survival. Proteasomes comprise a family of distinct complexes, which share a common proteolytic core, the 20S proteasome, but differ by their attached proteasome activators (1). Several proteasome activators have been identified which regulate proteasome function in distinct compartments and in a substrate-specific manner (2). The most prominent one is the 19S regulator that binds to the 20S proteolytic core either on one or both ends and mediates ATP- and ubiquitin-dependent protein degradation (3). Alternative proteasome activators including PA28αβ, PA28γ, and PA200 act ATP- and ubiquitin-independently and have distinct subcellular functions (1).

PA200, also known by its gene name PSME4, has been implicated in various cellular processes, such as DNA damage repair (4,5), mitochondrial and proteostatic stress responses (6,7), myofibroblast differentiation (8), aging (9,10) and protection from neuropathy (11,12). Recently, PA200 was found to be upregulated in NSCLC, where it restricted antigenic diversity of non-small cell lung cancer (NSCLC) tumors favoring immune evasion and responsiveness to immune checkpoint inhibition (13). Furthermore recent structural studies, such as the high-resolution cryo-EM analysis of PA200 bound to the human 20S proteasome complex, revealed that PA200 binds to the alpha rings of the 20S proteasome inducing conformational changes that modulate the activities of the catalytic subunits (14,15). Which of the active sites are activated by PA200, however, is controversial and several cellular studies presented conflicting results on the catalytic activation of the proteasome by PA200 (16). These data suggest a complex and context-dependent role for PA200 in regulating proteasomal function. Taken together, there is accumulating evidence that PA200 plays a role in multiple cellular functions that relate to tumor development and progression. Yet, our understanding of the cell autonomous function of PA200 in tumors and whether it can serve as a druggable target is still limited.

In this study, we conducted *in vitro* and *in vivo* analyses to investigate whether PA200 functions as an oncogene in lung cancer beyond its known role in modulating the immune escape of cancer cells. Our findings reveal that PA200 exhibits distinct functional roles in NSCLC cancer cells, including metabolic adaptation, invasion and migration, and tumor cell growth. Furthermore, our screening of a drug library identified Prest2-M17 as an inhibitor of

PA200-20S proteasome complexes *in vitro*. Our results collectively suggest that PA200 plays a unique role in tumor cell growth and migration and serves as a potential therapeutic target for cancer therapy.

RESULTS

Poor survival of lung cancer patients overexpressing PA200

To corroborate the potential oncogenic role of PA200 in lung cancer, we analyzed tissue expression of PA200 in different lung cancer types such as the main two forms of NSCLC, i.e., lung adenocarcinoma (LUAD) and squamous cell carcinoma (SQCLC), and compared it to expression in small cell lung cancer (SCLC) in a cohort of 60 patients. Paraffin-embedded tumor tissue was immunohistochemically stained for PA200, and signals were scored by an experienced pathologist in a blinded manner. We observed significantly increased expression of PA200 in LUAD and SQCLC compared to SCLC tumors (Figures 1A and B). Patients with high PA200 expression showed reduced survival compared to patients with low expression levels when PA200 expression levels were dichotomized into high versus low expressing tumors (Figure 1C). There was no statistical difference in PA200 expression level relative to tobacco smoke pack years, tumor or TNM stage (Suppl. Figures S1A-C). Our analysis thus provides immunohistochemical evidence for poor prognosis of NSCLC lung cancer patients with PA200 overexpression. It confirms previous data obtained with large RNA expression data sets (Javitt et al. 2023).

Generation of PA200 knockout NSCLC cell lines

To elucidate the functional role of PA200 in NSCLC, PA200 knock-out (KO) cell lines were generated using CRISPR/Cas9 technology. We used two distinct NSCLC cell lines, A549 and NCI-H1299 (hereinafter H1299), to determine the conserved function of PA200 in oncogenic cell growth and invasion. The two cell lines differ in their oncogenic mutations with A549 having an oncogenic K-Ras mutation, while H1299 contains a deletion of the tumor suppressor gene p53 and several N-ras mutations (https://www.cellosaurus.org). The epithelial and less invasive A549 cells were isolated from primary lung adenocarcinoma (17), whereas H1299 cells were derived from a metastatic lymph node and have a mesenchymal and invasive phenotype (18). We generated several PA200 KO clones in A549 and H1299 cell lines, as confirmed by RT-qPCR (Suppl. Figure S2A), DNA sequencing (Suppl. Figure S2C), Western blotting and native gel analysis (Figures 2A-B, Suppl. Figure S2B). We also found that H1299 cells express more PA200 than A549 cells as determined both for mRNA (Suppl. Figure S2A) and protein levels (Figure 1A) and have more PA200 bound to the 20S proteasome (Suppl. Figure S2B). In our native gel analysis, we observed that in PA200-depleted A549 cells the 20S

was more active regarding the CT-L activity compared to H1299 KO cells where the 20S activity was reduced while the 30S activity was elevated (Figure 2B). Deletion of PA200 in A549 cells reduced overall chymotrypsin-like (CT-L) and caspase-like (C-L) activities in total cell extracts compared to WT controls (Figure 2C). In H1299 cells, however, depletion of PA200 caused significant activation of both CT-L and C-L activities of the proteasome, while both cell lines had similar trypsin-like (T-L) activity levels (Figure 2C). These divergent effects of PA200 depletion on the complex-specific and overall proteasome activities might be due to the different levels of PA200 in the two cell types (see above) as well as to the altered binding of alternative proteasome activators such as PA28$\alpha\beta$ to the 20S in PA200-deleted A549 cells which is absent in PA200 H1299 KO cells (Figure 2D) contributing to an altered composition of the proteasome system in the two cell lines.

PA200 regulates migration and invasion of lung cancer cells

We tested the cellular effects of PA200 depletion in lung cancer cells by analyzing several hallmark pathways of cancer. Proliferation rates of A549 KO clones but not of H1299 KO cells were slightly lower than respective WT controls (Figure 3A). In contrast, the colony formation capacity did not change upon PA200 KO deletion in both cell lines (Suppl. Figures S3A). Under conditions of serum and glutamine deprivation, PA200 depleted A549 cells were more metabolically active within 72 hours than their WT control clones as determined by MTT assays (Figure 3B). Metabolic activity of H1299 PA200 KO cells, however, was reduced compared to PA200 WT cells (Figure 3B). These data suggest that PA200 depletion has variable effects on cell growth and proliferation in the two lung cancer cell lines. A common feature of PA200 depletion in both cell lines, however, was their reduced invasion capacity in wound healing and migration assays. Deletion of PA200 in A549 cells reduced invasion of matrigel-embedded A549 spheroids (Figure 3C), whereas two-dimensional migration of cells in scratch assays was not significantly altered (Figure 3E). Migration and invasion of PA200-depleted H1299 cells was strongly impaired, both in scratch and Boyden chamber assays compared to their WT control clones (Figures 3D and F). Expression of epithelial and mesenchymal marker genes was differentially regulated upon PA200 depletion in both cell lines (Figure 3G and Suppl. Figure S3B). The epithelial adherens junction marker E-cadherin and mesenchymal marker N-Cadherin were significantly upregulated at the protein level in A549 and H1299 PA200 KO cells indicating a partial epithelial-mesenchymal transition (EMT) state, while the

tight junction marker claudin was not regulated to a significant extent compared to WT controls. PA200 deletion did not affect expression of other mesenchymal markers, such as vimentin and β-catenin, in lung cancer cells. Of note, we observed strong and concerted downregulation of Integrin-β3 (ITGB3) expression in both PA200 depleted tumor cell lines (Figure 3G). ITGB3 encodes for the β3 subunit of integrins and serves as a major receptor for binding to different extracellular matrix (ECM) molecules. Taken together, our results indicate that PA200 plays a conserved role in the regulation of cell migration and invasion of NSCLC tumor cells but has also cell-specific effects that are possibly related to the cellular differentiation and proteasome composition as outlined above.

Transcriptional profiling of PA200 depleted tumor cells reveals conserved downregulation of metastasis related genes

To disentangle cell-specific from conserved effects of PA200 depletion, we performed unbiased transcriptional profiling of our WT and PA200 KO A549 and H1299 cell clones. PCA analysis highlighted the differences between the WT and KO clones (Suppl. Figures S4A-B). PA200 depletion had a stronger transcriptional effect in A549 compared to H1299 cells with 345 genes being down- and 419 up-regulated in PA200-depleted A549 cells and 288 genes down- and 196 genes up-regulated in H1299 PA200 KO clones (Figure 4A). To our surprise, we found only 16 genes being co-regulated in A549 and H1299 PA200 KO cells (highlighted in red and blue). Amongst the co-regulated, we detected besides PSME4, several proteins involved in cytoskeletal changes and organization as well as interaction with ECM. Amongst them we identified again Integrin-β3 (ITGB3) as a concertedly downregulated gene in both lung cancer cell lines as well as genes involved in cytoskeletal changes (PREX1, BICDL1), GPC1 as a heparan sulfate, the ankyrin binding protein ANKRD33B, and ADGRB1 (Adhesion G Protein-Coupled Receptor B1) involved in adhesion and cytoskeletal regulation. Reactome analysis of significantly regulated genes confirmed concerted downregulation of genes related to ECM formation such as collagen formation, ECM proteoglycans and integrin and surface organization-related genes, while several pathways involved in ECM degradation were upregulated both in A549 and H1299 PA200-depleted cells (Figures 4B-C).

Our transcriptional analysis thus confirms a conserved role for PA200 in the regulation of invasion and migration that is mediated by transcriptional regulation of integrins and ECM regulators. At the same time, the minimal overlap of the transcriptional response to PA200

depletion in the two NSCLC cell lines indicates that the function of PA200 is cell specific and depends on the cellular context.

PA200 depletion impairs tumor growth *in vivo*

To further analyze the cell-autonomous role of PA200 in lung cancer, we injected pools of the PA200 WT or KO A549 and H1299 cell clones into the flanks of immunocompromised SCID mice. Mice develop orthotopic tumors within 8 weeks and tumor growth and body weight was monitored daily (Suppl. Figures S5A-D). In this model, we can dissect the cell intrinsic role of PA200 in tumor development in the absence of its immune modulating function (13), as SCID mice are devoid of B and T cells and thereby lack adaptive immune responses. For A549 cells, we observed reduced flank tumor development in PA200 depleted cells (Figure 5A), while all mice developed tumors when injected with H1299 WT or PA200 KO cells (data not shown). Of note, deletion of PA200 significantly delayed tumor growth of both lung cancer cell lines up to 8 weeks (Figures 5B-C). Ki-67 staining of primary tumors did not reveal any significant difference in the number of proliferating cells between the WT and PA200-depleted tumors (Suppl. Figure S4E). We also carefully analyzed the lungs of tumor-bearing mice for macro- and micrometastases but did not find any metastatically spread tumor cells (data not shown). Most probably, the size and time restriction of primary tumor growth did not allow for their metastatic spread into the lungs. As tumor growth rates were reduced in the absence of PA200 and of an intact adaptive immune system, our results indicate that PA200 cell-autonomously alters tumor cell growth.

Identification of PA200/20S proteasome complex inhibitors

Our *in vitro* and *in vivo* data on the tumor-promoting role of PA200 prompted us to search for compounds that can specifically target 20S proteasomes that are bound to PA200. We therefore established an *in vitro* proteasome activation assay using immunopurified standard human 20S proteasomes (19) and recombinantly expressed human PA200 to assay the CT-L activity of the proteasome. We confirmed activation of the proteasome by increasing molar ratios of PA200 over 20S (0 to 8) (Figure 6A). PA200 was stably bound to the standard 20S proteasome, as determined by mass photometry (Figure 6B). As expected, increasing molar ratios of PA200 versus 20S progressively augmented the relative proportion of singly-capped (930 kDa) and doubly-capped (1,140 kDa) PA200-20S species, while decreasing the amount of

unbound 20S particles (720 kDa). At a molar ratio of 8, more than 60% of the total 20S was bound to PA200 (Figure 6C), in accordance with a 3-4-fold increase of the CT-L activity (Figure 6A).

These results prompted us to adjust our CT-L activity assay for high-throughput screening of potential inhibitory compounds of PA200:20S complexes using a PA200:20S molar ratio of 8 and free 20S for comparison. Among the 1,280 FDA-approved compounds from the Prestwick library that we tested for their effect on the CT-L activity of the PA200-bound versus free 20S (Suppl. Figure S6A and supplementary information for detailed description of the assay), one compound (Prest2-M17) was shown to significantly decrease the CT-L activity of PA200-activated 20S proteasome complexes by twofold at a final concentration of 10 µM (Figure 7A). This compound exerted significant specificity for PA200:20S complexes compared to free 20S (Suppl. Figure S6B). *In vitro* drug response curves for all three proteasomal activities on PA200-activated 20S proteasome complexes established the IC_{50} for this compound at 5-10 µM, 1-2 µM, and 100 µM for the CT-L, C-L, and T-L activities, respectively (Figures 7A-C). Of note, at a concentration of 0.5 µM, 30 ± 5% of the C-L activity of the PA200 activated 20S proteasomes was lost, while preserving more than 86 ± 5% of its CT-L and T-L activities *in vitro* (Figure 7D). Overall, the T-L activity seemed much less affected by the drug. We confirmed the inhibitory effects of the molecule on the CT-L and C-L activities *ex-cellulo* using cell lysates from HEK EBNA cells (Figure 7E). The Prest2-M17 compound is known as dequalinium chloride which is a well-known antiseptic drug with bactericidal activities and anti-cancer effects (20). We thus tested Prest2-M17 for its effect on tumor cell survival and invasion in A549 and H1299 cell lines. To identify potential PA200-mediated effects of the drug, we used the respective PA200 KO cells in a side-by side comparison. The compound showed cytotoxic effects on both WT and PA200 KO cell lines after 48 hours which were most pronounced at concentrations of 2.5 to 5 µM (Suppl. Figures S7A-B) according with published data (21). We next tested the compound in a wound healing assay for its activity on tumor cell migration. As demonstrated in Figure 7F, we observed significantly reduced migration in A549 WT cells already at doses of 0.5 µM, while H1299 cells showed only a tendency towards reduced wound healing (Figure 7, Suppl. Figures S7C-D). We did not observe any difference between WT and KO cells (Suppl. Figures 7C-D) suggesting that dequalinium chloride may act on additional cellular targets (20). Our proteasome activity data, however, suggest that dequalinium chloride might serve as a

potential hit for further Structure Activity Relationship (SAR) studies in order to increase its specificity towards PA200-proteasome complexes.

DISCUSSION

We here demonstrate that the proteasome activator PA200 regulates invasion and growth of NSCLC tumor cells *in vitro* and in vivo. These effects involve regulation of integrins and ECM regulators. At the same time our data reveal highly divergent cellular effects of PA200 depletion in epithelial-like versus mesenchymal-like cancer cell lines suggesting that PA200 functions as an intrinsic regulator of tumor cell function depending on the cellular context.

Role of PA200 in cancer

In cancer cells, PA200 has been shown to regulate glutamine sensitivity (22). PA200 KO mice do not develop tumors even when crossed to tumor suppressor p53 (Trpp53) deficient mice (23). However, transient overexpression of PA200 in KP1.9 tumor cells (KrasG12D; Trp53 deficient) and intravenous injection into mice gave rise to larger and significantly more tumor lesions whereas mice bearing PA200 silenced KP1.9 cells did not show any lesions (13). These effects were assigned to the escape from cytotoxic $CD8^+$ T cell immune control against PA200 overexpressing lung tumors thereby confirming a role for PA200 in regulating immunogenicity of NSCLC tumors (13). We here demonstrate that PA200 depleted NSCLC cancer cells show retarded growth behavior in an orthotopic xenograft mouse tumor model. The formation of tumors derived from allogenic human NSCLC cell injection into immunodeficient SCID mice rules out that the observed effects on reduced *in vivo* growth are mediated by modulation of cytotoxic $CD8^+$ T cells but rather point towards a cell intrinsic oncogenic role of PA200 in NSCLC. Moreover, we show that PA200 acts as a regulator of cell invasion as demonstrated by *in vitro* migration and invasion assays and the conserved downregulation of the integrin beta 3 (ITGB3) subunit both on RNA and protein level in two different NSCLC cell lines. Upregulation of ITGB3 is a well-established driver of metastasis in several solid cancer types and associates with poor prognosis (24–27). The ITGB3/FAK signaling hub also promotes growth factor signaling (28) which might explain the retarded growth of PA200-depleted tumor cells *in vivo*. Apart from this conserved role of PA200 in tumor cell invasion and growth, we noted a striking disparity of the effects of PA200 depletion in the two NSCLC cancer cell lines A549 and H1299. A major difference was already observed on the level of proteasome activity: While PA200 KO decreased the CT-L and C-L activities in A549 cells, these activities were increased in H1299 PA200 KO cells. The T-L activity was not altered. In-gel proteasome activity assays revealed a shift in proteasome complex composition with elevated amounts of 20S for PA200-depleted

A549 cells and decreased amounts of 26S/30S proteasome complexes in H1299 KO cells. As PA200 is expressed at rather low amounts in the cancer cells, we suggest that this differential shift in proteasome complex composition is not due to a direct effect of PA200 on complex formation but rather an indirect effect of adaptive proteasome remodeling in response to cellular changes upon PA200 depletion. This notion is supported by the observation that PA28αβ was recruited to 20S proteasome complexes in PA200-depleted A549 but not H1299 cells. We also observed an only minimal overlap in interacting proteins upon interactome analysis of PA200-pulldowns (data not shown). Indeed, the effect of PA200 depletion in A549 cells was clearly different from H1299 cells. A549 PA200 KO cells showed an elevated metabolic activity, while H1299 PA200 KO cells had reduced MTT activities (Figure 3B). Transcriptome analysis revealed striking differences in the transcriptional response to PA200 deletion in the two NSCLC cancer cell lines. Only 16 genes were co-regulated in A549 and H1299 PA200-depleted cells while 23 genes were even counter-regulated. Activation of Kras and inflammatory signaling were prominent features of PA200 depletion in A549 cells but these pathways were downregulated in H1299 PA200 KO cells. We have noticed such adaptive alterations of the proteasome system previously in primary human lung fibroblasts in response to TGF-β1-induced myodifferentiation upon transient knockdown of PA200 (8). Similarly, VerPlank et al. recently demonstrated that proteasomal degradation was activated in PA200 KO animals, contributing to protection from proteotoxic neuropathy (11). Taken together, there is accumulating evidence for an adaptive cellular response to PA200 depletion depending on the cellular context.

It is tempting to speculate that these divergent cell-type specific effects are related to the role of PA200 in DNA repair and histone degradation (4,5,29,30). This accords with the observation that inositol-6-phosphate (IP6), a nuclear regulator of enzyme function and DNA repair (31), is an integral component of PA200 as evidenced in structural analyses (14,15). PA200-dependent degradation of acetylated core histone was shown to occur primarily in actively transcribed regions that are hypomethylated (10). Any changes in the transcriptome and cellular function would thus be dependent on the existing epigenetic programming of the cell. Indeed, Jian et al. observed that the effect of PA200 depletion on the transcriptome was almost non-overlapping between liver tissue and mouse embryonic fibroblasts (10). This mechanism might thus explain the observed differential effects of PA200 in the two cancer cell lines.

Targeting PA200 for tumor therapy

Inhibitors of the proteasome inactivate the catalytic 20S core and effectively block protein degradation of all proteasome complexes in the cell resulting in growth inhibition and apoptosis (32). While these inhibitors, e.g. the FDA approved drugs Velcade™, Kyprolis™, Ninlaro™, have shown promising results in myeloma, their efficacy for solid tumors such as lung cancer is severely hampered by their pronounced cytotoxic side-effects due to broad inhibition of overall cellular protein degradation (32). Targeting of specific subpopulations of the proteasome might offer selective inhibition of defined protein degradation in the cell thereby inhibiting only distinct cancer-related cellular functions, i.e. survival, proliferation and migration. As only limited cytotoxicity is expected, this approach is thus highly favorable compared to broad and catalytic proteasome inhibition.

Our data together with the results of the Merbl lab (13) point towards a tumor-promoting role of PA200 in lung cancer that is related to its ability to regulate cell growth, migration and invasion as well as immunogenicity. This makes PA200 a potentially promising target for tumor therapy. We thus aimed to identify potential PA200 inhibitors, which can inhibit PA200-dependent activation of the 20S proteasome. In our drug screening approach, we tested 1,280 FDA-approved compounds with purified 20S and recombinantly expressed PA200 and identified Prest2-M17 as a candidate to inhibit the activities of PA200-20S complexes. Further, *ex-cellulo* studies with cell lines showed the ability of this ligand to inhibit both the standard and immunoproteasome (data not shown), the two main 20S proteolytic cores. Prest2-M17 also inhibited the migration of lung cancer cells, which recapitulated the KO of PA200. Our results demonstrate that this molecule might serve as a lead compound to reduce the proteolytic activation effect of PA200. A recent study reported the identification of a small molecule, I_3MO, that binds to the proteasome activators PA200 and PA28γ and could thereby sensitize multiple myeloma cells to the anti-tumor effects of the proteasome inhibitor Bortezomib (33). They did not, however, perform *in vitro* experiments on purified complexes as done in our study to show specific and direct proteasome inhibition by the compound, so that one cannot rule out indirect effects on the proteasome.

In summary, this study highlights the intricate and context-dependent role of PA200 in NSCLC, influencing invasion and tumor growth and suggests potential therapeutic approaches targeting PA200-20S complexes.

MATERIALS AND METHODS

Reagents

Standard 20S proteasome was purified in-house (see detailed protocol below). The substrates for proteasome activity assay were purchased from Bachem (Suc-LLVY-AMC), while Boc-LRR-AMC and z-LLE-AMC were purchased from Enzo Life Science.

Preparation of recombinant human PA200

The PA200 gene was optimized for Spodoptera frugiperda expression, ordered from GenScript and cloned into a pFastBact1 vector with an N-terminal cleavable 6-Histidine tag. Recombinant Baculovirus was produced using the Bac-to-Bac system into Sf21 cells using EMBACY cells (34). One Liter of Sf21 cells ($1x10^6$ cell/mL) was infected with 10mL of virus, and cells were harvested after 72 h. Thawed cells were resuspended in buffer A (50 mM Tris-HCl pH 8, 500 mM NaCl, 10 mM imidazole, 2 mM β-Mercaptoethanol (mEtOH) supplemented with protease inhibitor cocktail and DNAse I), lysed by sonication and centrifuged at 45 000 x g for 1 h. Supernatant was passed through Nickel columns equilibrated with buffer A three times, followed by wash with the same buffer. Protein was eluted with buffer B (50 mM Tris-HCl pH 8, 500 mM NaCl, 300 mM imidazole, 2 mM β-mEtOH), mixed with TEV protease and dialysed overnight against buffer C (50 mM Tris-HCl pH 7.5, 100 mM NaCl, 2 mM β-mEtOH). The next day, the protein solution was loaded onto a Q sepharose HP column equilibrated with buffer D (50 mM Tris-HCl pH 7.5, 2 mM β-mEtOH) and eluted with a gradient of buffer E (50 mM Tris-HCl pH 7.5, 1 M NaCl, 2 mM β-mEtOH). Fractions containing PA200 were pooled, concentrated and loaded onto Superdex 200 Increase 10/300 GL column equilibrated with buffer F (50 mM Tris-HCl pH 7.5, 100 mM NaCl, 2 mM β-mEtOH). Purified protein was concentrated to 1 mg/ml and used for preparation of cryo-EM samples and other *in vitro* assays.

Animal experiments

The experimental procedures involved NOD/SCID (strain code 394) mice purchased from Charles River and experiments were performed according to local regulations in Bavaria, Germany (TVA approval number ROB-55.2-2532.Vet_02-20-197). Male and female animals were used in the experiments, the sample size was determined beforehand through a G*power analysis and experimental procedures were randomized across different cages. The

animals were anaesthetized before being injected with $3x10^6$ PA200 WT or PA200 KO cells in 150 µl PBS, and their body weight and tumor size were measured regularly. Mice had to be sacrificed once their tumor burden reached the maximal size, the primary tumor had necrosis or 10 weeks after the cell injection. Once the endpoint conditions were met, the mice were euthanized using lethal anaesthesia for organ harvesting and further examinations.

Cell culture and generation of knockout cell lines

The human NSCLC cell lines were obtained from DSMZ or were a gift from Dr. Georgios Stathopoulos. The cell lines were cultured at 37˚C and 5% CO_2 in a humidified incubator. A549 cells were grown in DMEM/F12 medium, while NCI-H1299 cells were cultured in RPMI-1640 medium, both supplemented with 10% FBS and 100 U/mL penicillin/streptomycin. For serum deprivation, 1% FBS medium was used.

Low passage number cells were harvested at 80% confluency. Transfection of TrueCut Cas9 Protein v2, Hs.Cas9.PSME4.1.AB and tracRNA (IDT) was performed using the Lipofectamine CRISPRMAX Transfection Reagent protocol. The cells were incubated at 37°C for 48 h after transfection. Following the incubation period, the cells were collected, and 50 cells were seeded onto 15 cm dishes. After 2 weeks, colonies were picked with trypsin-incubated cloning disks and transferred to 24-well (one colony per well). To confirm the knockout efficiency, protein and DNA were isolated. For PCR-based amplification and sequencing the following primer were used:

Application	**Species**		**Sequence 5´- 3´**
PCR	Human	Forward	ATCTGCAAGAGAGATGCAGCC
	Human	Reverse	AGGTTTGAGCAGCAGCAAGA
Sanger Sequencing	Human	Reverse	TGGATGGGGAAAGCAAAACCC

Cell proliferation, metabolic activity and colony formation assays

The proliferation rate of different cell types was assessed using established methodology (35,36). A549 (30,000 cells/well) and NCI-H1299 (40,000 cells/well) cells were seeded into 6-well plates. The initial cell count was determined on day 1, and the final cell count was recorded on day 4 to calculate the rate of cell division per day according to the formula below:

$$Proliferation\ Rate = \frac{log2(\frac{Final\ day\ cell\ count(Day\ 4)}{Initial\ day\ cell\ count\ (Day\ 1)})}{(Final\ day - Initial\ day\ (3\ Day))}$$

Cellular metabolic activity was assessed using the MTT assay. Cells were cultured in 24-well plates and incubated with a thiazolyl blue tetrazolium bromide solution (Sigma). The resulting formazan product was measured at 570 nm using a plate reader (Tecan). A colony formation assay was conducted by seeding 100 NCI-H1299 and 200 A549 cells in 6-well plates as previously described (37). The culture medium was refreshed on day 3 and day 7. On day 10, the cells were fixed using 4% formaldehyde, stained with 1% crystal violet dye (Sigma), photographed, and quantified.

Live/dead staining

To determine the toxicity of the Prest2-M17 inhibitor on A549 and H1299 cancer cell lines, we performed flow cytometry-based live/dead staining. Pools of A549 and H1299 WT and PA200 KO cell lines were plated into 24 well plates (15,000 A549 cells/well; 20,000 H1299 cells/well) 24 h before treatment with the drug (1 mM stock solution dissolved in sterile H2O, Sigma) at the indicated concentrations (0.5 µM, 1 µM, 2.5 µM, 5 µM) for 24 and 48 h and compared to solvent-treated and untreated controls. Cells were trypsinized and collected in 100 µl FACS staining buffer (1 x DPBS, 2% FCS, 0.1% sodium azide, 0.2mM EDTA) and distributed into 96 well plates. 100 µl FACS staining buffer containing propidium iodide (Calbiochem) with an end concentration of 1 µg/ml was added and the samples were measured in the MACSQant Analyzer 16 (Miltenyi Biotec). Cell Counts were analyzed with Flowlogic software.

Migration and invasion assays

For Boyden chamber migration analysis, a 10% FBS medium was used as a chemoattractant in 24-well plates. Boyden chambers (Biotrend) containing 100,000 NCI-H1299 cells in 0% FBS medium were inserted into the wells. After 24 hours, the cells were fixed with 4% formaldehyde and stained with 1% crystal violet solution. Excess dye was washed off, and the chambers were left to dry before imaging with Axio Observer.Z1/7 (Zeiss) or the BioTek Cytation 1 (Agilent).

For wound healing assays, inserts (Ibidi, Germany) were used to assess cellular wound healing capacity. The inserts were placed into a 24-well plate (1 insert/well), with A549 (28,000

cells/insert side) and NCI-H1299 (20,000 cells/insert side) cells seeded on both sides. Inserts were removed after 24 h and 1 ml of medium was added. For experiments related to Figure 4 cells were incubated in a live cell imaging microscope (Axio Observer.Z1/7) at 37°C and 5% CO2 for 48h or until the 500 µm gap closed. Images from different time points were calculated using the Wound Healing Tool macro on ImageJ (38). For experiments relating to Figure 7, cells were treated with 0.5 µM and 1 µM Dequalinium chloride (1 mM stock solution dissolved in sterile H_2O, Sigma), stained with CellTox™ Green Dye (1:2,000 dilution, Promega) and imaged in a live cell imaging multimode reader (Cytation1, Agilent Technologies, Inc., USA) at 37°C and 5% CO_2 for 48 h. Using a 4x objective, one to two images per well were captured at different time points using bright field and GFP imaging channels. If two pictures were taken, the images were stitched prior to analysis. Images were analyzed regarding the wound area, wound width, and average wound closure rate using the Gen5 3.16 Software (Agilent Technologies, Inc., USA) following the application note "Incorporation of a Novel, Automated Scratch Tool and Kinetic Label-Free Imaging to Perform Wound Healing Assays" by Brad Larson (Agilent Technologies, Inc., USA).

For gel invasion assays, a total of 5,000 A549 cells were seeded in low attachment U-bottom 96-well plates (Neolab) with 100 µl of medium and centrifuged briefly for 2 minutes at 1,000 rpm to establish initial cell-cell contact. The cells were then incubated for 72 h under standard conditions. After this incubation period, the spheroids were gently collected into 1.5 ml Eppendorf tubes and allowed to settle on the tube's bottom for 5 min on ice. Subsequently, a collagen G matrix gel was prepared, as described previously (39). Briefly, solution A was created by combining 1M HEPES buffer (pH= 7-7.5) and 0.7M NaOH in equal proportions. Solution A was mixed with 20% FBS in 10× PBS (pH = 7.4) in a 1:1 ratio to create solution B (pH = 7.90–8.05). For the final gelation step, collagen G and solution B were mixed in a 4:1 ratio (v:v). To create a collagen G+Matrigel matrix, a mixture of collagen G matrix gel and Matrigel was prepared in a 1:1 ratio (v:v). The spheroids were transferred into the matrix mixture and placed in an incubator to solidify over a period of 5 h. After solidification, the spheroids were imaged using a live cell imaging microscope for 72 h.

Western Blot analysis

Denatured protein extracts were generated with the RIPA lysis buffer (50 mM Tris/HCl pH 7.5, 50 mM NaCl, 1% IGEPAL, 0.5% Sodium deoxycholate, 0.1% SDS). Briefly, frozen cell pellets

were dissolved in RIPA buffer supplemented with protease inhibitor (Roche Diagnostics) and phosphatase inhibitor (Roche Diagnostics). The cell lysis process was carried out on ice and lasted for 20 minutes, with periodic vortexing during this period. Subsequently, the lysates were centrifuged at 15,000 rpm and 4°C for 20 minutes to remove cellular debris. Protein concentrations were calculated with BCA assay according to manufacturer's recommendation (Pierce BCA Protein Assay Kit, Thermo Fisher) and 15 µg protein extracts were diluted with Milli-Q® water and mixed with 6x Laemmli buffer to a final concentration of 1x. Samples were denatured at 95 °C for 15 min. Polyacrylamide gels were prepared and cast using Bio-Rad equipment (Bio-Rad, Germany). Denatured protein extracts were loaded on the gel and electrophoresis was performed at 90 - 120 V.

Proteins were transferred to a methanol-activated PVDF membrane at 250 mA for 90 minutes at 4°C. Membranes were blocked with Roti®-Block (1 h) or EveryBlot (10 min). Primary antibodies were incubated overnight at 4°C, followed by three 15-min PBST washes. HRP-conjugated secondary antibodies were applied for 1 h at room temperature. After two PBST washes, chemiluminescence was detected using Luminata™ or SuperSignal reagents with iBright CL1500 (ThermoFisher) or ChemiDoc (Bio-rad) systems. Densitometric analysis was conducted using ImageLab software.

Table 1: List of antibodies

Target	Catalog Number	Host & Type	Working Dilution	Company
Claudin-1 (D5H1D)	13255	Rb mAb	1:1,000	Cell Signaling Technology
E-Cadherin (24E10)	3195	Rb mAb	1:1,000	Cell Signaling Technology
Integrin β3 (ITGB3)	D7X3P	Rb mAb	1:1,000	Cell Signaling Technology
N-Cadherin (D4R1H)	13116	Rb mAb	1:1,000	Cell Signaling Technology
PA200	NBP1-22236	Rb pAb	1:5,000	Novus Biologicals
Vimentin (D21H3)	5741	Rb mAb	1:1,000	Cell Signaling Technology
α1-7 (MCP231)	ab22674	Ms mAb	1:1,000	Abcam

β-Actin (HRP-linked)	A3854	Ms mAb	1:8,0000	Sigma-Aldrich
β-Catenin (D10A8)	8480	Rb mAb	1:1,000	Cell Signaling Technology
Anti-goat IgG HRP-linked	61-1620	Rb	1:40,000	Thermo Fisher Scientific
Anti-mouse IgG HRP-linked	7076	Hs	1:40,000	Cell Signaling Technology
Anti-rabbit IgG HRP-linked	7074	Hs	1:40,000	Cell Signaling Technology

Rb: Rabbit, **Ms**: Mouse, **Gt**: Goat, **mAb**: Monoclonal, **pAb**: Polyclonal

In-gel proteasome activity assay

Native gel electrophoresis was performed to analyze intact and active proteasome complexes, following previously optimized and detailed protocol (40). Briefly, frozen cell pellets were thawed and lysed in OK lysis buffer (50 mM Tris/HCl pH 7.5, 2 mM DTT, 5 mM MgCl2, 10% glycerol, 2 mM ATP, 0.05% digitonin) supplemented with protease and phosphatase inhibitors (Roche Diagnostics). Cells were lysed on ice for 20 min with intermittent vortexing, followed by centrifugation at 15,000 rpm for 20 min at 4°C. Protein concentration was determined by BCA assay, and 15 µg of protein was diluted with water, mixed with 5x native gel loading buffer, and loaded onto 3-8% gradient NuPAGE Novex Tris-acetate gels (Life Technologies). Electrophoresis was performed at 150 V for 4 h at 4°C in native gel running buffer. Following electrophoresis, an in-gel proteasome activity assay was conducted to assess chymotrypsin-like (CT-L) activity using an activity buffer (50 mM Tris, 1 mM ATP, 10 mM $MgCl_2$, 1 mM DTT, and 0.05 mM Suc-LLVY-AMC). Fluorescence was detected using the ChemiDoc XRS+ system (BioRad). For immunoblotting, gels were incubated in solubilization buffer (2% SDS, 66 mM Na_2CO_3, 1.5% β-mEtOH) for 15 min before protein transfer.

Total proteasome activity assay

The activity of the 20S proteasome's active sites—chymotrypsin-like (CT-L), caspase-like (C-L), and trypsin-like (T-L)—was evaluated using the Proteasome-Glo™ Assays (Promega, Fitchburg), following the manufacturer's instructions. In brief, 1 µg of protein from OK lysates was mixed with OK lysis buffer (see above) to ensure equal volumes, and the final volume was

adjusted to 20 µL with water. These dilutions were transferred to white flat-bottom 96-well plates and combined with 20 µL of the specific substrates. Luminescence was measured at 2-min intervals over 45 min using a Tristar LB 941 plate reader (Berthold Technologies). Each sample was analyzed in quadruplicate, and the plateau values of the luminescent signal were used for quantifying proteasome activity for each specific substrate.

Immunohistochemical analysis of mice and human tissues

Excised mice tissue specimens were fixed in a 4% (w/v) solution of formalin, followed by paraffin embedding and sectioning into slices measuring 3 µm thick. These sections were subsequently stained using hematoxylin and eosin (HE) staining. The staining procedure was carried out using the HistoCore SPECTRA ST automated slide stainer (Leica, Germany) with ready-made staining reagents (Histocore Spectra H&E Stain System S1, Leica, Germany) following the instructions provided by the manufacturer. Immunohistochemical staining was performed following standardized protocols on a Discovery Ultra automated stainer (Ventana Medical Systems, Tucson, AZ). Polyclonal rat anti-Ki67 (1:1,000, Abcam, Cambridge, UK) was used as a primary antibody. Signal detection was achieved using the Discovery® DAB Map Kit (Ventana Medical Systems, Tucson, AZ). The stained tissue sections were then digitally scanned using an AxioScan.Z1 digital slide scanner (Zeiss) equipped with a 20x magnification objective.

Human lung tissue obtained from patients surgically treated for lung cancer was provided by the Asklepios Biobank for Lung Disease, Gauting, Germany. Samples were approved with ethical consent obtained by the ethics committee of the Ludwig-Maximilians University Munich according to national and international guidelines (project number 333-10).

Paraffin embedded human tissues were cut in 3 µm thick sections using the Hyrax M55 microtome (Zeiss). Tissue sections were incubated for one hour at 60 °C in order to melt paraffin, deparaffinized by incubating two times in xylene for 5 min and rehydrated in a descending alcohol series (100 %, 90 %, 80 % and 70 % (v/v)) for 1 min. To block endogenous protease activity and to permeabilize sections for nuclear staining they were incubated in a methanol/hydrogen peroxide (80 %/1.8 % (v/v)) solution for 20 min. Tissue sections were rinsed in Milli-Q® water and heat-induced antigen retrieval was performed in citrate buffer pH 6 using a decloaking chamber (Biocare Medical). After washing with TBST unspecific binding sites were blocked for 30 min with Rodent Block M (Biocare Medical). The slides were

washed again in TBST and incubated with anti-PA200 antibody (sc-135512, Santa Cruz) diluted in Antibody Diluent (DAKO) for 1 h at RT. After extensive washing in TBST, sections were incubated with MACH 2 Rabbit AP-Polymer (Biocare Medical) for 30 min at RT. Sections were rinsed again in TBST and incubated in Vulcan Fast Red AP substrate solution (Biocare Medical) for 10 min. Tissue sections were washed in TBST and MilliQ® water and hematoxylin counterstaining (Carl Roth) was performed to visualize nuclei. After repeated washing in TBST, sections were dehydrated in ethanol and xylene and mounted using Entellan mounting medium (Merck Millipore). Slides were imaged using the MIRAX scanning system (Zeiss). Stainings were analyzed by an expert clinical pathologist blinded to the sample identity. Semiquantitative scores for PA200 expression were obtained by defining the percentage of PA200 positively stained tumor areas multiplied by the intensity of staining as graded between 1 (weak) to 3 (strong). Scores were dichotomized into high (>80) and low (<80) expressing tumors with the score 80 representing the median of all samples and PA200 expression scores were correlated with survival of the patients for this cohort.

RNA isolation

For RT-qPCR, cellular RNA was isolated using the Roti®-Quick Kit (Roth) via phenol-chloroform extraction according to manufacturer's instructions. Briefly, cells were lysed in Quick 1 solution, followed by the addition of Quick 2 solution. Samples were incubated on ice for 10 minutes, then centrifuged at 10,000 rpm and 4°C for 15 min to separate phases. The upper aqueous phase was carefully collected and transferred to a new tube and Quick 3 solution was added. The samples were incubated either at -80°C for 40 min or at -20°C overnight. RNA was pelleted by centrifugation at 13,000 rpm and 4°C for 20 min, followed by washing twice with 70% ethanol. The RNA pellet was air-dried on ice and reconstituted in 25-40 µL of nuclease-free water

For bulk RNA sequencing, RNA was isolated using an RNA isolation kit (VWR, Germany) according to the provided protocol. Cell pellets were lysed in TRK buffer with 2% β-mEtOH and homogenized using a peqGOLD RNA Homogenizer Column (VWR). Following centrifugation at ≥12,000 x g for 2 min, the flow-through was mixed with ethanol (70%) and vortexed. The mixture was then passed through a peqGOLD RNA Mini Column via centrifugation at 10,000 x g for 1 min. The column was washed with RNA Wash Buffer I and 80% ethanol, followed by

centrifugation steps to remove residual ethanol. RNA was eluted by nuclease-free water and concentration was determined using the NanoDrop 1000 (ThermoFisher).

Reverse transcription of RNA and RT-qPCR

For the reverse transcription process, RNA ranging from 0.25 to 1 µg was mixed with 9 µL of nuclease-free water, followed by the addition of 2 µL of 250 µM Random Hexamers (Thermo Fisher Scientific). After allowing the mixture to incubate at 70 °C for 10 min, the samples were placed on ice. Subsequently, 9 µL of a reverse transcription master mix was introduced, with final concentrations of 1x First Strand Buffer, 10 mM DTT, 0.5 mM dNTPs, 1 U/µL RNAse Inhibitor, and 10 U/µL M-MLV transcriptase. The reverse transcription procedure involved annealing for 5 min at 25°C, followed by elongation for 60 min at 37°C, which was executed using a Mastercycler Nexus (Eppendorf). The cDNA was subjected to digestion with 1 U of DNase at 37°C for 15 min, followed by heat inactivation at 75°C for 10 min. The resultant cDNA was then diluted at a 1:5 ratio with nuclease-free water (Ambion, Thermo Fisher Scientific).

Quantitative real-time RT-PCR analysis was carried out using the SYBR Green LC480 system from Roche. A mixture comprising 2.5 µL of both forward and reverse primer dilutions (0.5 µM each) and 5 µL of LC480 SYBR Green I Master mix (Roche) was prepared per well in a 96-well plate format. Additionally, 2.5 µL of cDNA was added to each well. Each sample was measured in duplicate, and the plates were centrifuged for 2 minutes at 1,000 rpm prior to initiating the measurements using the standard program outlined in Table 4.7 on the Light Cycler 480 II (Roche). The gene expression levels of the various samples were normalized to the housekeeping gene ribosomal protein L19 (RPL19). The relative gene expression was determined using the ΔΔCT method, with the specificity of the primers verified by analyzing the melting curve.

List of Primers: FW: Forward primer, **RV**: Reverse Primer

Target Gene	**Target Species**		**Sequence 5'-3'**
B-catenin	human	FW	CATCTACACAGTTTGATGCTGCT
		RV	GCAGTTTTGTCAGTTCAGGGA

claudin 2 (CLDN2)	human	FW	ATCGCTCCAACTACTACGATGC
		RV	TGAACTCACTCTTGACTTTGGGA
E-Cadherin (CDH1)	human	FW	ATTTTTCCCTCGACACCCGAT
		RV	TCCCAGGCGTAGACCAAGA
ITGB3	human	FW	CATGAAGGATGATCTGTGGAGC
		RV	AATCCGCAGGTTACTGGTGAG
N-Cadherin (CDH2)	human	FW	AGCCAACCTTAACTGAGGAGT
		RV	GGCAAGTTGATTGGAGGGATG
PSME4	human	FW	ATTTGGAGTTACCCTGGAGACC
		RV	GCAGCTTTTCACGAGTGTTTTG
RPL19	human	FW	TGTACCTGAAGGTGAAGGGG
		RV	GCGTGCTTCCTTGGTCTTAG
Vimentin (VIM)	human	FW	TGCCGTTGAAGCTGCTAACTA
		RV	CCAGAGGGAGTGAATCCAGATTA

Bulk mRNA sequencing

A total of 1.5 million A549 cells and 1 million H1299 cells were cultured in 15 cm dishes and incubated for 48 hours. Total RNA was isolated utilizing the Total RNA kit (Peqlab, VWR). Subsequently, the samples were dispatched to the Core Facility Next-Generation Sequencing at the Helmholtz Center Munich. The RNA integrity number (RIN) was assessed using the Agilent 2100 Bioanalyzer system, and concentration was quantified using the Qubit 2.0 RNA BR assay (Invitrogen). RNAs with RIN values exceeding 6 were chosen for total RNA sequencing (ribo-depleted), a method that effectively detects essential coding and non-coding transcripts by removing highly abundant rRNA species.

Library preparation for both human and mouse samples involved using the TruSeq stranded total-RNA Library Preparation kit (Illumina) with 1 µg of RNA, following the kit's protocol. Following a final quality control step, the libraries were subjected to paired-end sequencing (2x150 bases) on the Hiseq 4000 sequencer (Illumina), targeting a depth of at least 40 million

paired reads per sample. Subsequent to sequencing, initial processing (demultiplexing) of raw data to fastq files was performed using the bcl2fastq v2.20 program from Illumina.

For RNA sequencing file alignment, the STAR tool was employed with the GRCh38/hg38 version. To estimate transcript abundances, the FeatureCounts function within the Subread2 package was utilized in the Unix environment. Initially, the gene-code ReleaseM23 (GRCm38.p6) served as the gene annotation. Subsequently, data underwent filtering, normalization, and differential gene expression analysis using relevant packages within the R programming environment.

limma: (https://bioconductor.org/packages/release/bioc/html/limma.html)

edgeR: (https://bioconductor.org/packages/release/bioc/html/edgeR.html)

Purification of 20S from HEK-EBNA cells

Human HEK293-EBNA cells expressing only 20S, previously described in (19) were grown in Iscove's Modified Dulbecco's Medium (IMDM) supplemented with 10% fetal bovine serum (FBS), 116 mg/l L-arginine and 36 mg/l L-asparagine. Medium was replaced every 2-3 days and cell passaging was done at around 80% confluence. The cells were washed with Dulbecco's phosphate-buffered saline (DPBS) three times and stored at -80 °C until use.

Large scale purification of proteasomes was done using MCP21 antibody grafted to Cyanogen bromide-activated Sepharose beads, as described earlier (41). The purification was done at 4 °C or in an ice bath. Cells were lysed with lysis buffer at pH 7.6 containing 20 mM Tris-HCl, 0.25% TritonX-100, 100 mM NaCl, 10 mM EDTA, and 1 tablet of protease and phosphatase inhibitors per 50 mL (cOmplete™ ULTRA Tablets Mini EDTA-free and PhosSTOP, Roche Diagnostics) and sonicated with Vibracell (10 cycles, 30 sec on and 1 min off, 50% active cycle). The lysate was centrifuged at 16,000 g for 30 min then the supernatant was filtered through a 0.22 µm membrane. The filtered lysate was then mixed with the beads grafted with MCP21 antibody and incubated overnight. The next day, the beads were washed with equilibration buffer (20 mM Tris HCl, 1 mM EDTA, 10% glycerol, 100 mM NaCl, pH 7.6) and eluted with equilibration buffer supplemented with 3 M NaCl.

The eluate was concentrated down to 0.5 mL on centrifugal filters of 100 kDa MWCO and then separated using gel filtration chromatography. The chromatography was performed on a Superose 6 10/300 GL column, using TSDG buffer (10 mM Tris-HCl pH 7.0, 1 M KCl, 10 mM NaCl, 5.5 mM MgCl2, 0.1 mM EDTA, 1 mM DTT, 10% glycerol). The fractions were assayed by

proteasome enzymatic activity and the active proteasome fractions (eluted fractions between 10 - 14 mL) were pooled together. Buffer exchange with equilibration buffer and concentration of fractions were done on centrifugal filters of 100 kDa MWCO (VivaspinTM, Cytiva). Additional glycerol was added to reach 20% and smaller aliquots were made. Aliquots were snap-frozen in liquid nitrogen and stored at -70 °C until use.

Activation of 20S with PA200

The ability of our recombinant PA200 to associate and to activate the 20S was checked by two orthogonal methods, i.e measurement of the chymotrypsin-like activity, and assessment of the distribution of the different macromolecular complexes by mass photometry. s20S with and without PA200 were analyzed at different PA200:s20S molar ratios, from 0 to 8 and the two protein complexes were incubated for at least 30 min.

For proteolytic activity assessment, 20 µL of each protein complex (to reach a final concentration of 1.75 nM 20S) was pipetted in a 384-well plate. Then, 20 µL of substrate solution in 50 mM Tris-HCl pH 7.5 (final concentration of 200 µM) was added in the corresponding wells. The plate was centrifuged at 1,500 g for 20 sec and was put in a microplate fluorimeter (CLARIOstar, BMG Labtech) for the measurement. Fluorescence intensity was measured at Ex 350-15 nm/ Em 400-20 nm at 37 °C for every 5 min for at least 12 cycles. Gain and focal height were adjusted before the measurement. Also, orbital shaking was done for two seconds after each cycle at 100 rpm. The slope on the linear range (fluorescence intensity vs. time) was calculated for all the wells. To get the relative activation, the slope was then normalized with the average slope for the control (i.e. c20S only, i.e molar ratio of 0). Details on the ligand screening to identify PA200/20S proteasome complex inhibitors can be found in the supplement.

Mass photometry analysis

Protein complexes were prepared by mixing 20S with PA200 at different molar ratios in 50 mM Tris-HCl pH 7.5 buffer. The solutions were incubated for about 15 min at room temperature. Analysis in the mass photometer (Refeyn Ltd) was done according to the manufacturer's protocol. Calibration was initially done with NativeMarkTM Unstained Protein Standard (Thermo Scientific). In a gasket well, 17.5 µL of the buffer was loaded for focusing. 2.5 µL of protein sample was loaded and mixed with the buffer and acquisition was done for

60 sec. The fraction of occupied 20S binding sites was calculated as the sum of counts of singly- and doubly-capped complexes divided by 2 x the total counts of 20S (i.e. sum of 20S, singly-capped, and doubly-capped). The fraction of occupied 20S binding sites (y-axis) was plotted with the experimental molar ratio (x-axis).

Statistical analysis

The specific statistical analyses for each panel are provided in the corresponding figure legends. Statistical significance was denoted in the figures as follows: * for $p < 0.05$, ** for $p < 0.01$, *** for $p < 0.001$, or **** for $p < 0.0001$. The figures display data as mean ± SEM. All statistical analyses were performed using GraphPad Prism software (version 10).

ACKNOWLEDGEMENT

The study was supported by a BMBF grant to SM and GP (16GW0287) and a DFG/ANR grant to SM and MPB (ME2002/6-1 and ANR-PA200_IN_IPF). The acquisition of the mass photometer was supported by an INCA grant (OncoRib) to JM. The ligand screening assay was supported by a Toulouse Tech Transfer prematuration grant to JM and MPB. We are grateful to Marijke Jansma and Grzegorz Popowicz from the Helmholtz Center Munich to provide us with human recombinant PA200.

CONTRIBUTIONS

ASY, FK, LZ, ASD, DZ, GGG, SB performed experiments; ASY, DZ, ASD, LZ, GGG, SB, ESP, TG, GTS and NR analyzed the data; ASY, SM, MPB, JM wrote and revised the manuscript; SM, JM, MPB developed and coordinated the project.

REFERENCES

1. Wang X, Meul T, Meiners S. Exploring the proteasome system: A novel concept of proteasome inhibition and regulation. Pharmacology & Therapeutics. Elsevier Inc.; 2020;107526.

2. Coux O, Zieba BA, Meiners S. The Proteasome System in Health and Disease. Advances in experimental medicine and biology. 2020;1233:55–100.

3. Bard JAM, Goodall EA, Greene ER, Jonsson E, Dong KC, Martin A. Structure and Function of the 26S Proteasome. Annual review of biochemistry. 2018;87:697–724.

4. Blickwedehl J, Agarwal M, Seong C, Pandita RK, Melendy T, Sung P, et al. Role for proteasome activator PA200 and postglutamyl proteasome activity in genomic stability. Proceedings of the National Academy of Sciences of the United States of America. 2008;105:16165–70.

5. Blickwedehl J, McEvoy S, Wong I, Kousis P, Clements J, Elliott R, et al. Proteasomes and Proteasome Activator 200 kDa (PA200) Accumulate on Chromatin in Response to Ionizing Radiation. Radiation Research. 2007;167:663–74.

6. Douida A, Batista F, Robaszkiewicz A, Boto P, Aladdin A, Szenykiv M, et al. The proteasome activator PA200 regulates expression of genes involved in cell survival upon selective mitochondrial inhibition in neuroblastoma cells. J Cell Mol Med. 2020;24:6716–30.

7. Welk V, Coux O, Kleene V, Abeza C, Truembach D, Eickelberg O, et al. Inhibition of Proteasome Activity Induces Formation of Alternative Proteasome Complexes. Journal of Biological Chemistry. 2016;291:jbc.M116.717652.

8. Welk V, Meul T, Lukas C, Kammerl IE, Mulay SR, Schamberger AC, et al. Proteasome activator PA200 regulates myofibroblast differentiation. Scientific Reports. 2019;9:15224.

9. Lin C, Li H, Liu J, Hu Q, Zhang S, Zhang N, et al. Arginine hypomethylation-mediated proteasomal degradation of histone H4—an early biomarker of cellular senescence. Cell Death Differ. 2020;27:2697–709.

10. Jiang T-X, Ma S, Han X, Luo Z-Y, Zhu Q-Q, Chiba T, et al. Proteasome activator PA200 maintains stability of histone marks during transcription and aging. Theranostics. 2021;11:1458–72.

11. VerPlank JJ, Gawron JM, Silvestri NJ, Wrabetz L, Feltri ML. Knockout of PA200 improves proteasomal degradation and myelination in a proteotoxic neuropathy. Life Sci Alliance. 2024;7:e202302349.

12. Aladdin A, Yao Y, Yang C, Kahlert G, Ghani M, Király N, et al. The Proteasome Activators Blm10/PA200 Enhance the Proteasomal Degradation of N-Terminal Huntingtin. Biomolecules. 2020;10:1581.

13. Javitt A, Shmueli MD, Kramer MP, Kolodziejczyk AA, Cohen IJ, Radomir L, et al. The proteasome regulator PSME4 modulates proteasome activity and antigen diversity to abrogate antitumor immunity in NSCLC. Nat Cancer. 2023;4:629–47.

14. Toste Rêgo A, da Fonseca PCA. Characterization of Fully Recombinant Human 20S and 20S-PA200 Proteasome Complexes. Molecular Cell. 2019;76:138-147.e5.

15. Guan H, Wang Y, Yu T, Huang Y, Li M, Saeed AFUH, et al. Cryo-EM structures of the human PA200 and PA200-20S complex reveal regulation of proteasome gate opening and two PA200 apertures. Walters KJ, editor. PLoS Biol. 2020;18:e3000654.

16. Yazgili AS, Ebstein F, Meiners S. The Proteasome Activator PA200/PSME4: An Emerging New Player in Health and Disease. Biomolecules. 2022;12:1150.

17. Sundararajan R, Salameh T, Camarillo IG, Prabu RR, Natarajan A, Sankaranarayanan K. Irreversible electroporation: a drug-free cancer treatment. Electroporation-Based Therapies for Cancer [Internet]. Elsevier; 2014 [cited 2024 Dec 16]. page 219–43. Available from: https://linkinghub.elsevier.com/retrieve/pii/B9781907568152500108

18. Tripathi SC, Peters HL, Taguchi A, Katayama H, Wang H, Momin A, et al. Immunoproteasome deficiency is a feature of non-small cell lung cancer with a mesenchymal phenotype and is associated with a poor outcome. Proceedings of the National Academy of Sciences. 2016;201521812.

19. Guillaume B, Chapiro J, Stroobant V, Colau D, Van Holle B, Parvizi G, et al. Two abundant proteasome subtypes that uniquely process some antigens presented by HLA class I molecules. Proceedings of the National Academy of Sciences of the United States of America. 2010;107:18599–604.

20. Bailly C. Medicinal applications and molecular targets of dequalinium chloride. Biochemical Pharmacology. 2021;186:114467.

21. Bae Y, Jung MK, Lee S, Song SJ, Mun JY, Green ES, et al. Dequalinium-based functional nanosomes show increased mitochondria targeting and anticancer effect. European Journal of Pharmaceutics and Biopharmaceutics. 2018;124:104–15.

22. Blickwedehl J, Olejniczak S, Cummings R, Sarvaiya N, Mantilla A, Chanan-Khan A, et al. The Proteasome Activator PA200 Regulates Tumor Cell Responsiveness to Glutamine and Resistance to Ionizing Radiation. Mol Cancer Res. 2012;10:937–44.

23. Khor B, Bredemeyer AL, Huang CC-Y, Turnbull IR, Evans R, Maggi LB, et al. Proteasome Activator PA200 Is Required for Normal Spermatogenesis. Molecular and cellular biology. 2006;26:2999–3007.

24. Parvani JG, Gujrati MD, Mack MA, Schiemann WP, Lu Z-R. Silencing β3 Integrin by Targeted ECO/siRNA Nanoparticles Inhibits EMT and Metastasis of Triple-Negative Breast Cancer. Cancer Research. 2015;75:2316–25.

25. Cheng C, Liu D, Liu Z, Li M, Wang Y, Sun B, et al. Positive feedback regulation of lncRNA TPT1-AS1 and ITGB3 promotes cell growth and metastasis in pancreatic cancer. Cancer Science. 2022;113:2986–3001.

26. Zepp JA, Morley MP, Loebel C, Kremp MM, Chaudhry FN, Basil MC, et al. Genomic, epigenomic, and biophysical cues controlling the emergence of the lung alveolus. Science. 2021;371:eabc3172.

27. Lei Y, Huang K, Gao C, Lau QC, Pan H, Xie K, et al. Proteomics Identification of ITGB3 as a Key Regulator in Reactive Oxygen Species-induced Migration and Invasion of Colorectal Cancer Cells. Molecular & Cellular Proteomics. 2011;10:M110.005397.

28. Yoon S, Yang H, Ryu H-M, Lee E, Jo Y, Seo S, et al. Integrin αvβ3 Induces HSP90 Inhibitor Resistance via FAK Activation in KRAS-Mutant Non-Small Cell Lung Cancer. Cancer Res Treat. 2022;54:767–81.

29. Qian M-X, Pang Y, Liu CH, Haratake K, Du B-Y, Ji D-Y, et al. Acetylation-Mediated Proteasomal Degradation of Core Histones during DNA Repair and Spermatogenesis. Cell. 2013;153:1012–24.

30. Mandemaker IK, Geijer ME, Kik I, Bezstarosti K, Rijkers E, Raams A, et al. DNA damage-induced replication stress results in PA200-proteasome-mediated degradation of acetylated histones. EMBO reports. 2018;e45566.

31. Kefala Stavridi A, Gontier A, Morin V, Frit P, Ropars V, Barboule N, et al. Structural and functional basis of inositol hexaphosphate stimulation of NHEJ through stabilization of Ku-XLF interaction. Nucleic Acids Research. 2023;51:11732–47.

32. Manasanch EE, Orlowski RZ. Proteasome inhibitors in cancer therapy. Nature Reviews Clinical Oncology. Nature Publishing Group; 2017;14:417–33.

33. Yu Z, Wei X, Liu L, Sun H, Fang T, Wang L, et al. Indirubin-3'-monoxime acts as proteasome inhibitor: Therapeutic application in multiple myeloma. eBioMedicine. 2022;78:103950.

34. Trowitzsch S, Bieniossek C, Nie Y, Garzoni F, Berger I. New baculovirus expression tools for recombinant protein complex production. Journal of Structural Biology. 2010;172:45–54.

35. Meul T, Berschneider K, Schmitt S, Mayr CH, Mattner LF, Schiller HB, et al. Mitochondrial Regulation of the 26S Proteasome. Cell reports. 2020;32:108059.

36. Sullivan LB, Gui DY, Hosios AM, Bush LN, Freinkman E, Vander Heiden MG. Supporting Aspartate Biosynthesis Is an Essential Function of Respiration in Proliferating Cells. Cell. Elsevier Inc.; 2015;162:552–63.

37. Franken NAP, Rodermond HM, Stap J, Haveman J, Van Bree C. Clonogenic assay of cells in vitro. Nat Protoc. 2006;1:2315–9.

38. Carpentier G, Berndt S, Ferratge S, Rasband W, Cuendet M, Uzan G, et al. Angiogenesis Analyzer for ImageJ — A comparative morphometric analysis of “Endothelial Tube Formation Assay” and “Fibrin Bead Assay.” Sci Rep. 2020;10:11568.

39. Burgstaller G, Oehrle B, Koch I, Lindner M, Eickelberg O. Multiplex profiling of cellular invasion in 3D cell culture models. PloS one. 2013;8:e63121.

40. Yazgili AS, Meul T, Welk V, Semren N, Kammerl IE, Meiners S. In-gel proteasome assay to determine the activity, amount, and composition of proteasome complexes from mammalian cells or tissues. STAR Protoc. 2021;2:100526.

41. Bousquet-Dubouch M-P, Baudelet E, Guérin F, Matondo M, Uttenweiler-Joseph S, Burlet-Schiltz O, et al. Affinity purification strategy to capture human endogenous proteasome complexes diversity and to identify proteasome-interacting proteins. Molecular & cellular proteomics : MCP. 2009;8:1150–64.

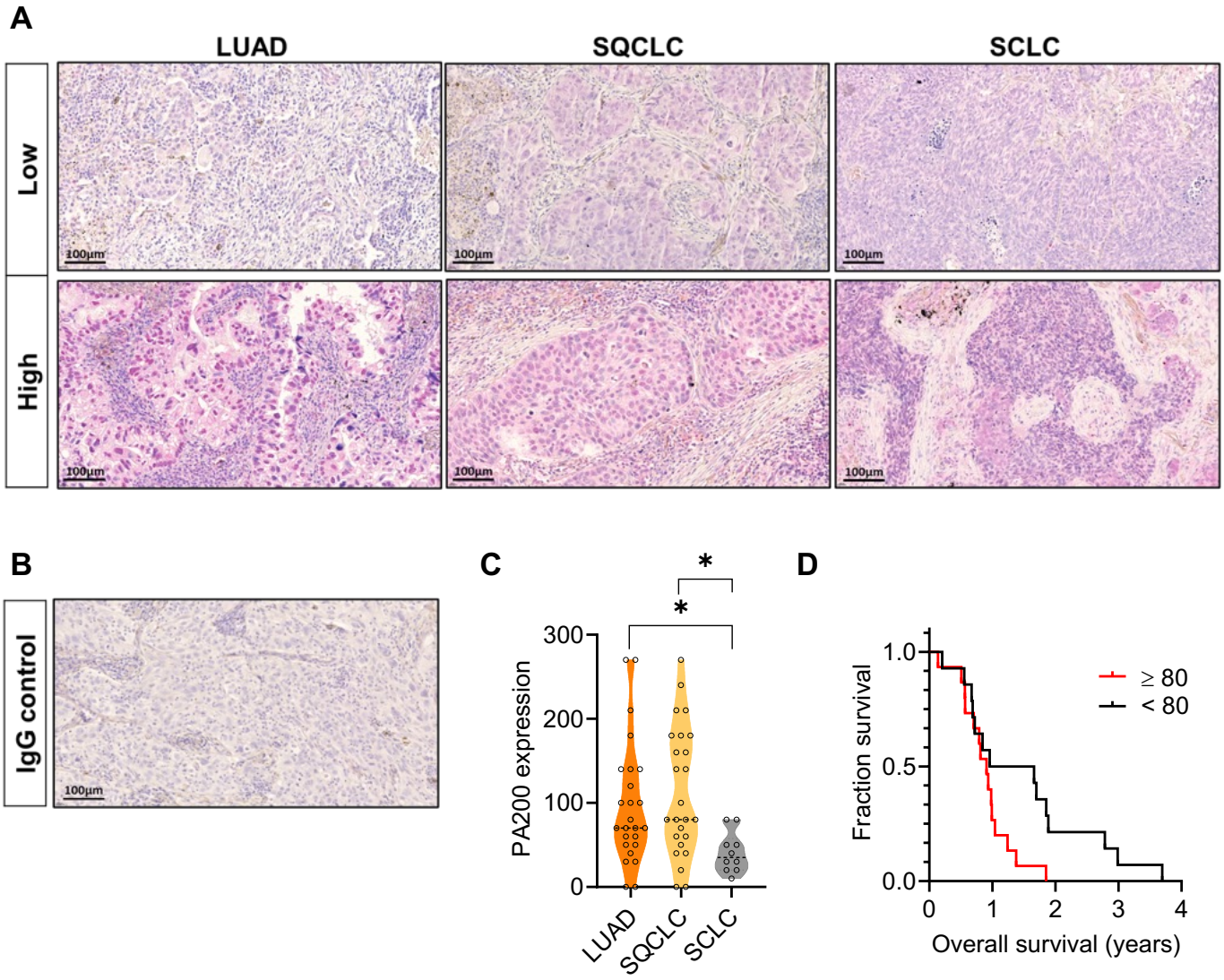

Figure 1: Increased PA200 levels positively associated with lung cancer patient survival. A) Representative images of tumor sections in LUAD, SQCLC, and SCLC. **B)** Representative image of IgG control in LUAD tissue **C)** Immunohistochemical analysis of tumor sections (24 LUAD, 14 SQCLC, 9 SCLC), semiquantitatively graded by a blinded pathologist (Kruskal Wallis, Dunn's multiple comparisons test) **D)** Analysis of overall survival (Log-rank Mantel-Cox test, n=29. p>0.05).

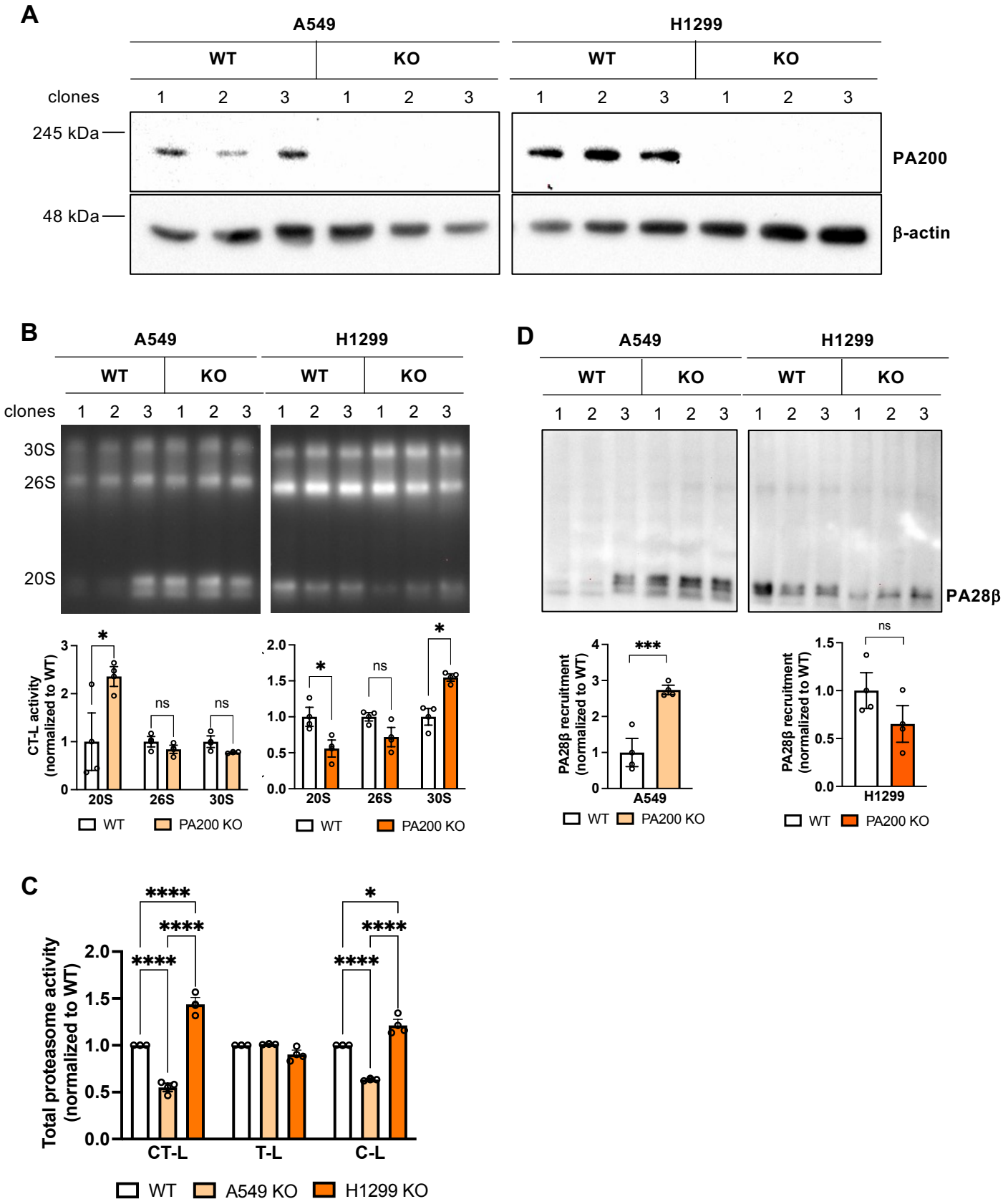

Figure 2: Knock-out of PA200 in lung cancer cell lines differentially affects proteasome activity. PA200 protein-depleted cell lines were generated by CRISPR/Cas9 in A549 and H1299 cell lines. **A)** PA200 protein expression levels as determined by Western blotting. β-actin served as a housekeeping protein to ensure equal protein loading. **B)** in-gel proteasome CT-L activity and **C)** total proteasome activity of CT-L, T-L and C-L were analyzed in the different clones and normalized to the respective WT control clones. **D)** Binding of PA28αβ to the proteasome was assessed by blotting native gels with an anti-PA28β antibody (*$p < 0.05$, **$p < 0.01$, ****$p < 0.0001$, ordinary 2 way ANOVA, n=3).

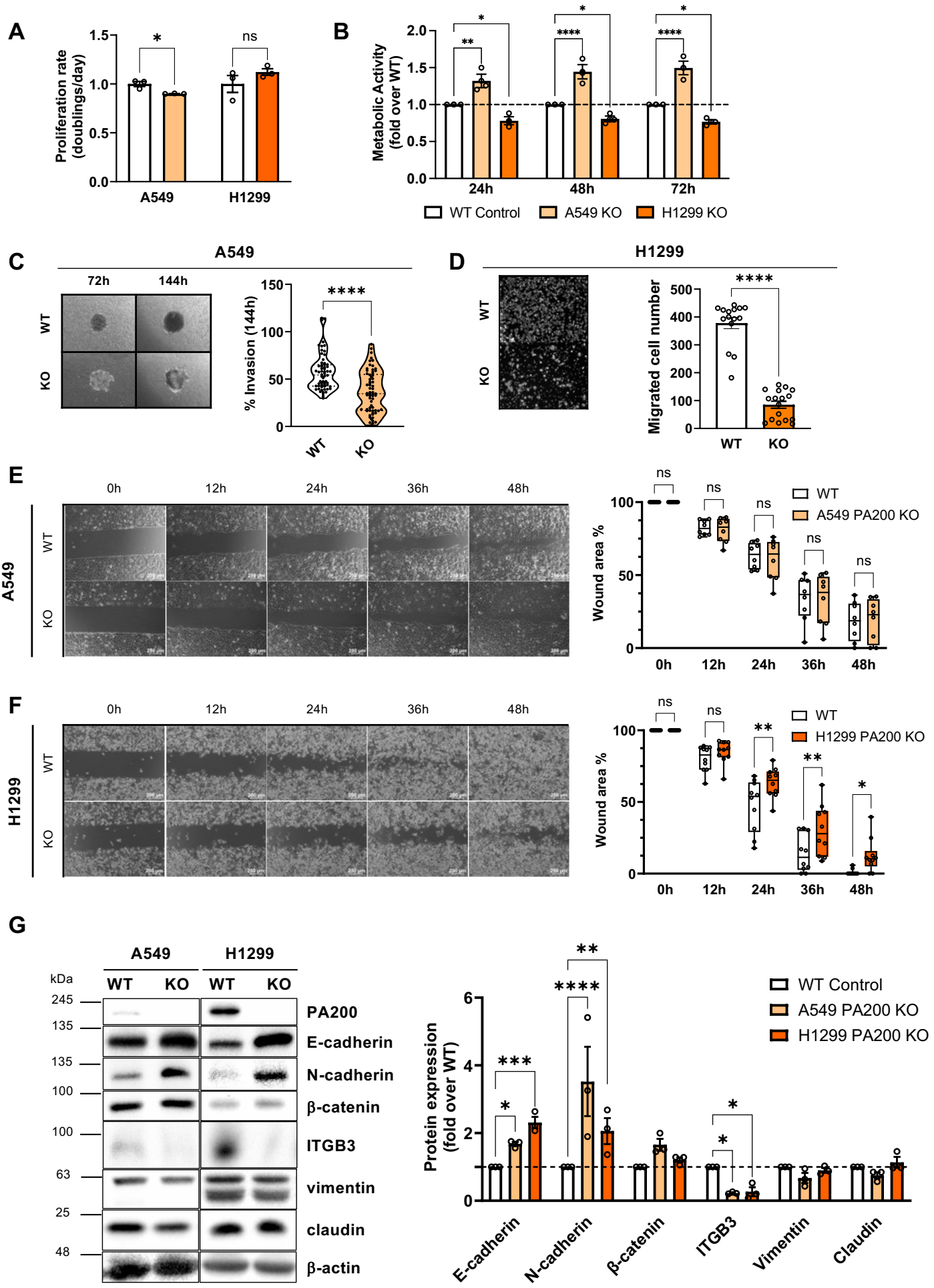
A
Proliferation rate (doublings/day)
1.5
1.0
0.5
0.0
*
ns
A549
H1299
B
Metabolic Activity (fold over WT)
2.0
1.5
1.0
0.5
0.0
*
**
*
****
*
****
24h
48h
72h
WT Control
A549 KO
H1299 KO
C
A549
72h
144h
WT
KO
% Invasion (144h)
150
100
50
0
****
WT
KO
D
H1299
WT
KO
Migrated cell number
500
400
300
200
100
0
****
WT
KO
E
A549
0h
12h
24h
36h
48h
WT
KO
Wound area %
100
50
0
ns
WT
A549 PA200 KO
0h
12h
24h
36h
48h
F
H1299
0h
12h
24h
36h
48h
WT
KO
Wound area %
100
50
0
ns
**
**
*
WT
H1299 PA200 KO
0h
12h
24h
36h
48h
G
A549
H1299
kDa
WT
KO
WT
KO
245
135
135
100
100
63
25
48
PA200
E-cadherin
N-cadherin
β-catenin
ITGB3
vimentin
claudin
β-actin
Protein expression (fold over WT)
6
4
2
0
**
****
***
*
*
*
WT Control
A549 PA200 KO
H1299 PA200 KO
E-cadherin
N-cadherin
β-catenin
ITGB3
Vimentin
Claudin

Figure 3

Figure 3: Depletion of PA200 differentially alters proliferation, migration and invasion in NSCLC cell lines. A) Pools of three A549 and H1299 WT and KO cell clones were seeded and counted on different days to track the doubling time. The data were normalized to the respective WT control. (n=3, different passages, unpaired t-test). **B)** MTT assay was used to determine the metabolic activity rates in A549 and H1299 pools of WT and KO clones under 1% serum and L-glutamine starvation (n=3, different passages, ordinary 2 way ANOVA). **C)** An 3D invasion assay was employed for A549 WT and KO cell pools to determine their invasive capacity. Representative images of the spheroids after 72 h of initial seeding and 72 h after embedding in the Collagen G+Matrigel membrane (left panel). The invasion percentage was calculated by comparing the 72h and 144 h area differences (right panel, n=3, different passages). **D)** Representative images of the Boyden chamber migration assay of the H1299 cells (left panel) and quantifications (right panel) are shown (n=3, different passage, two-tailed unpaired t-test). Representative photos of the wound closures of **(E)** A549 and **(F)** H1299 WT and KO cells were taken every 12 h up to 48 h and quantified (right panel, ordinary 2way ANOVA, n=3, different passages). **G)** Protein levels of epithelial and mesenchymal markers were quantified (right panel, n=3, different passages, 2 way ANOVA) in A549 and H1299 WT and KO pools and β-actin (representative image) served as protein loading control. For quantification, relative expression levels were normalized to the respective WT controls. *$p < 0.05$, **$p < 0.01$, ***$p < 0.001$, ****$p < 0.0001$.

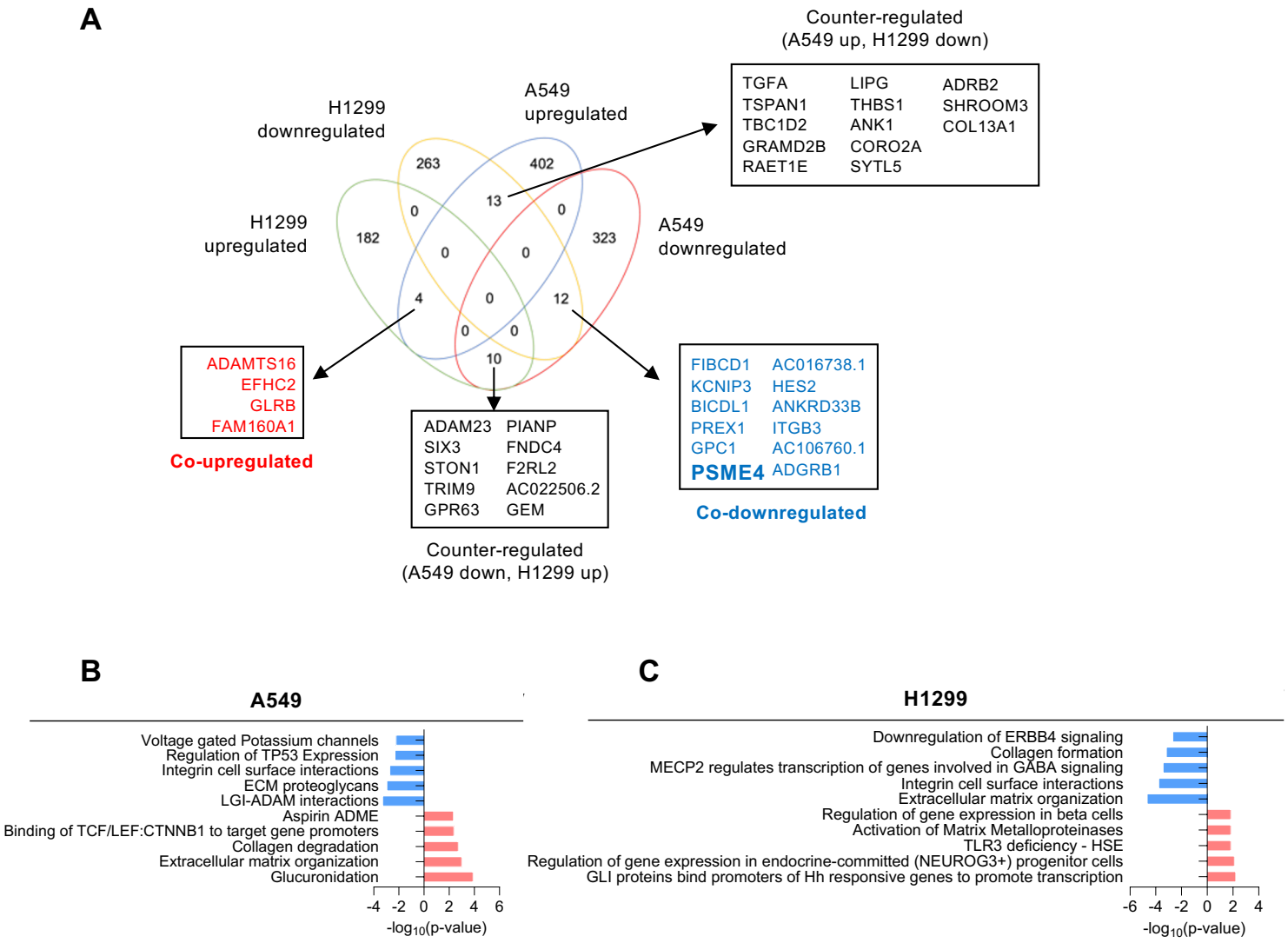

Figure 4: RNA sequencing analysis of PA200 KO in NSCLC cell lines reveals differential regulation of the transcriptome upon PA200 depletion. The effects of PA200-depletion in A549 and H1299 on transcriptional regulation was analyzed by RNA sequencing. **A)** The results were filtered (|FC| ≥ 2, p ≤ 0.05, FDR ≤ 0.05) and a Venn diagram was used to show the co-regulated and counter-regulated genes. Reactome analysis showed the significantly up (pink) or down (blue) regulated pathways in **(B)** A549 and **(C)** H1299 cells. (n=3, WT and KO).

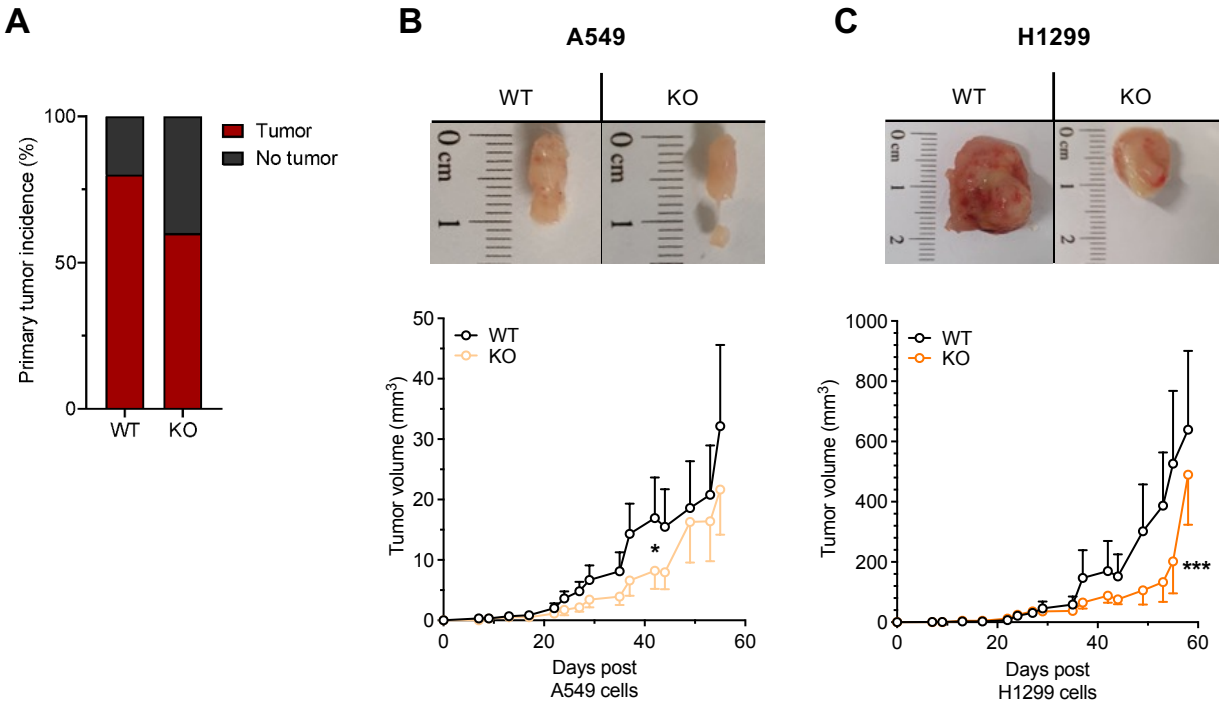

Figure 5: Reduced tumor growth upon PA200 depletion in two NSCLC cell lines. A549 and H1299 WT and PA200 KO cell pools were injected subcutaneously into SCID mice and measured in size after dissection. **A)** Primary tumor incidence for A549 cells. **B)** Primary tumor volumes of A549 and **(C)** H1299 cells were monitored over time (ordinary 2 way ANOVA, WT cells injected into 10 mice and PA200 KO cells injected into 15 mice). (*$p < 0.05$, ***$p < 0.001$).

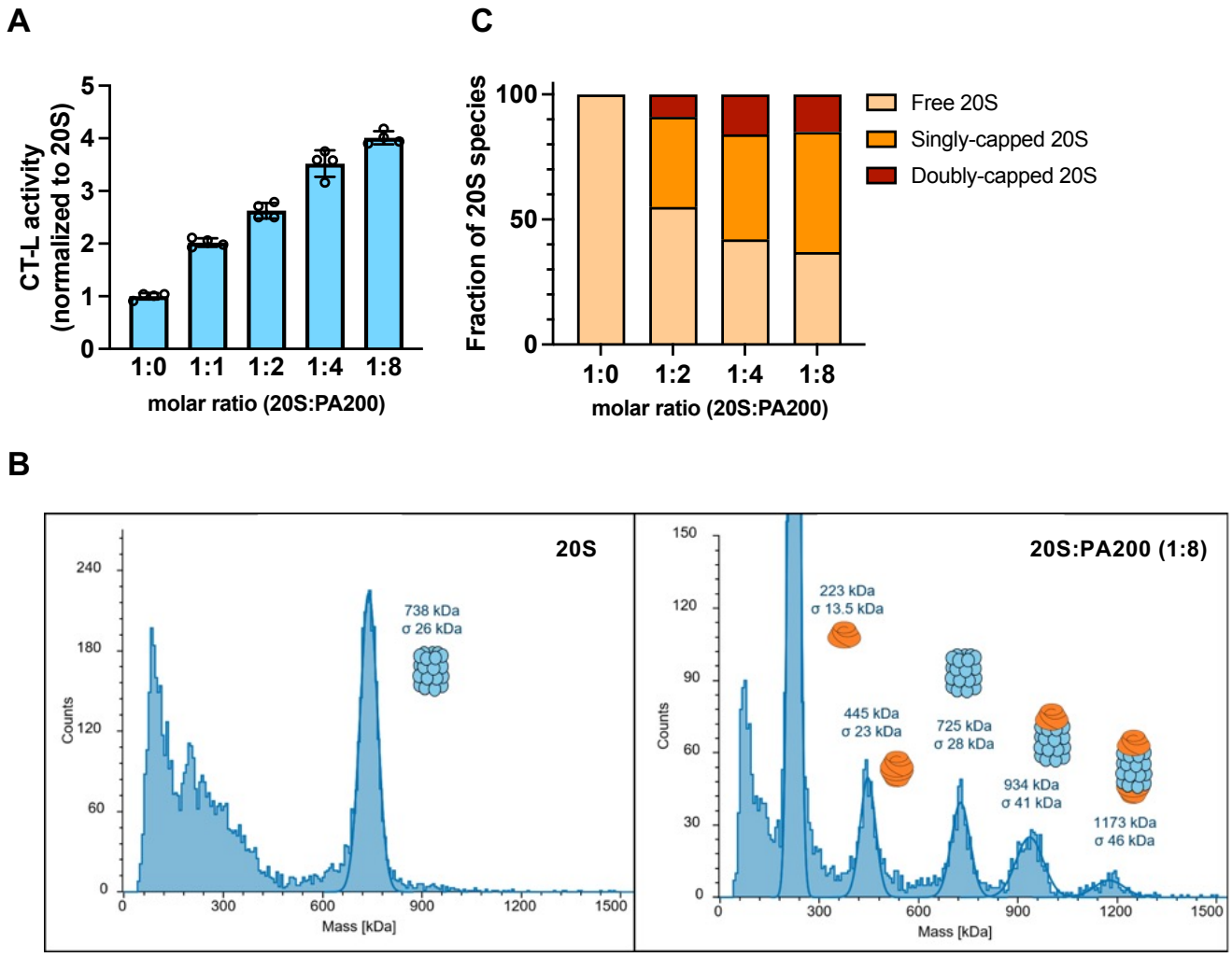

Figure 6: Recombinant PA200 binds and activates purified 20S proteasomes in a concentration-dependent manner. A) Activation of 20S by the PA200 activator. Different PA200 over 20S molar ratios were used (from 0 to 8) and the level of CT-L activation was monitored using the LLVY-AMC substrate. The data were normalized to the average activity of the 20S control (20S:PA200 ratio of 1:0). **B)** Mass histograms of 20S and its associated PA200 activator with 20S alone (left) and PA200 at a molar excess of 8-fold showing the different species pertaining to the 20S alone at ap. 720 kDa, PA200 singly-capped proteasomes at ap. 930 kDa, and PA200 doubly-capped proteasomes at ap. 1,140 kDa. Estimated mass and standard mass deviations (sigma) are displayed above the histograms. **C)** Proportions of free 20S, singly-capped 20S, and doubly-capped 20S at different PA200:20S ratios as determined by mass photometry. The 20S occupancy increases with the activator to 20S ratio.

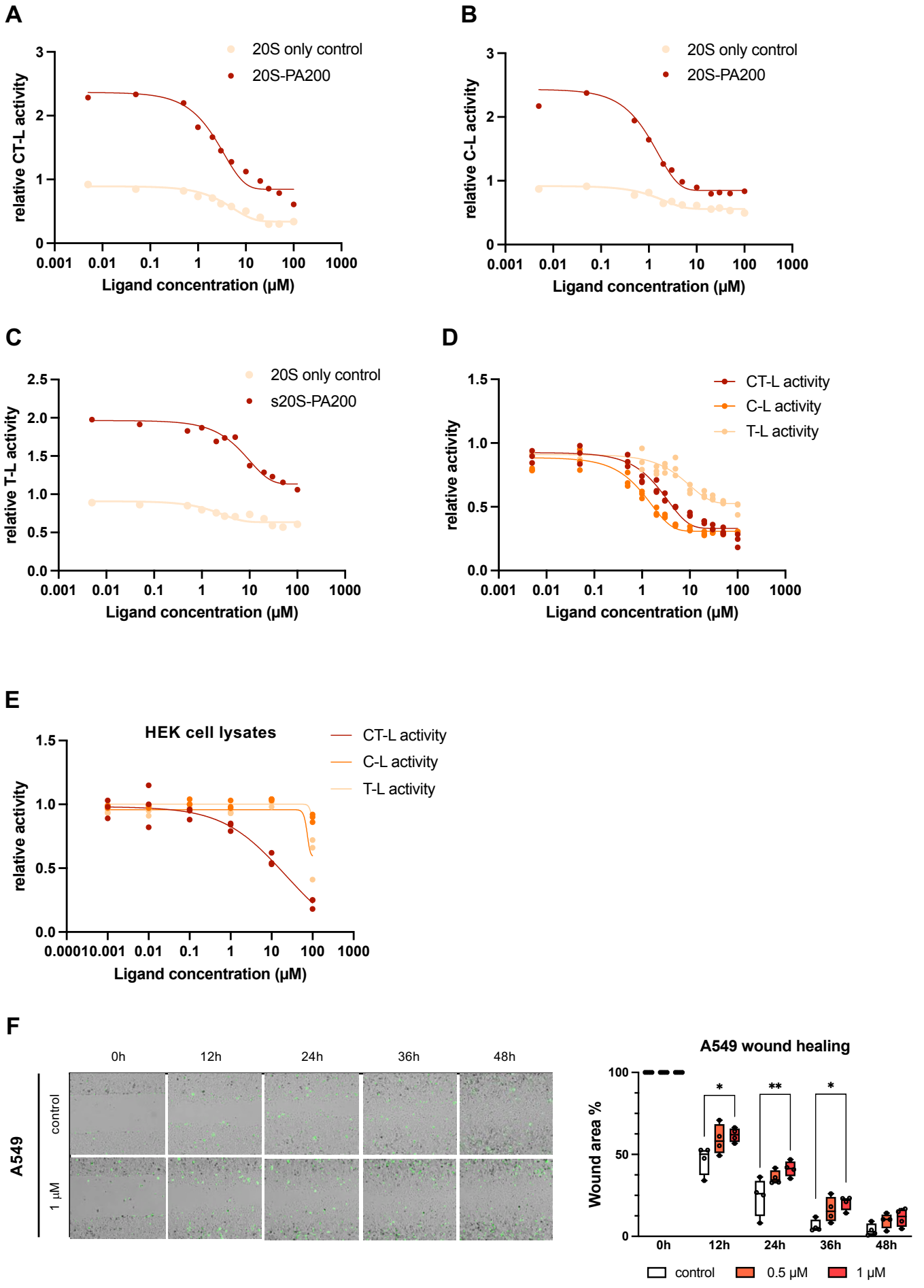
A
20S only control
20S-PA200
relative CT-L activity
Ligand concentration (μM)
B
20S only control
20S-PA200
relative C-L activity
Ligand concentration (μM)
C
20S only control
s20S-PA200
relative T-L activity
Ligand concentration (μM)
D
CT-L activity
C-L activity
T-L activity
relative activity
Ligand concentration (μM)
E
HEK cell lysates
CT-L activity
C-L activity
T-L activity
relative activity
Ligand concentration (μM)
F
0h
12h
24h
36h
48h
A549
control
1 μM
A549 wound healing
Wound area %
control
0.5 μM
1 μM

Figure 7

Figure 7: Inhibitory activity of the Prest2-M17 ligand. Dose response curves of the Prest2-M17 inhibitor *in vitro* using purified 20S proteasomes alone and bound to recombinant human PA200 at PA200:20S molar ratios of 8 or 0 (i.e. free 20S) **(A-D)** and *ex-cellulo* using cell lysates from HEK EBNA cells **(E)**. The three proteasomal activities, i.e. chymotrypsin-like (CT-L) **(A, E)**, caspase-like (C-L) **(B, E)** and trypsin-like (T-L) **(C, E)** activities, were tested using the LLVY, LLE, and LRR fluorogenic peptides, respectively. The Prest2-M17 ligand was added at a final concentration from 0 to 100 µM and data were obtained in triplicates. Measured activities were normalized to the activity of the free 20S proteasome **(A-C)** or to the DMSO control **(D, E)**. **F)** A549 and H1299 WT and PA200 cells (pools of three single clones each) were labeled with CellTox™ Green Dye to identify dying cells (in green) and treated with Prest2-M17 for 48 h after removing the insert. Representative photos of the wound closures of A549 WT cells were taken every 12 h up to 48 h (shown only for 1 mM Prest2-M17) and quantified (right panel, ordinary 2way ANOVA, n=4 independent experiments) using the Gen5 3.16 Software (Agilent Technologies, Inc., USA).